The apparent friction of granular fault gouge in sheared layers

David R. Scott[1]

Southern California Earthquake Center, University of Southern California, Los Angeles

Chris J. Marone

Department of Earth, Atmospheric and Planetary Sciences
Massachusetts Institute of Technology, Cambridge

Charles G. Sammis

Department of Geological Sciences, University of Southern California, Los Angeles

Abstract. Data are presented from a series of experiments on layers of granular quartz gouge in the double-direct-shear geometry at a normal stress of 25 MPa. The apparent friction of a layer, defined as the ratio of the applied shear and normal stresses, shows considerable variability depending on the thickness of the layer and the particle size distribution of the gouge. Measurements of layer thickness during the experiments also show that the layers thin as shearing proceeds. Layer thinning is attributed to the processes of extrusion and densification, and by analyzing these processes the observed variations in apparent friction are reconciled with a constant coefficient of internal friction for quartz gouge. For thinning due only to extrusion, the prinicipal assumption made is that the deviatoric stress and plastic strain rate are coaxial. When densification is also admitted, a simple flow law with one adjustable parameter is required to relate the volumetric and shear strain rates. The results and analysis show that (1) extrusion and densification must be considered when interpreting the measured frictional properties of gouge layers; (2) shear localization is inhibited in these experiments; and (3) the apparent friction of a natural fault zone may be less than $\sin \phi$, where $\tan \phi$ is the coefficient of internal friction of gouge in the fault zone.

Introduction

Natural faults are in general marked not by a sharp planar contact between walls of intact country rock but rather by a finite layer of damaged fault rock. Fault gouge, a granular material found in many fault zones, is formed by fragmentation of the intact country rock as the fault develops. Shear motion may be accommodated by distributed strain in the gouge layer or by slip on localized surfaces within the gouge; in either case, the frictional properties of the fault zone are presumably controlled by the gouge.

A distinction can be made between granular gouge and clay gouge. In granular gouge, the mineralogy of the country rock (typically dominated by quartz) is unchanged, although a large proportion of the gouge is very fine grained. In clay gouge, the mineralogy of the gouge is also substantially altered from that of the country rock. This study is concerned with the mechanical behavior of granular gouge.

A number of experimental studies of rock friction have been directed toward assessing the effect of a gouge layer on the frictional properties of a simulated fault zone. The experimental geometries used include double-direct-shear [*Dieterich*, 1981; *Biegel et al.*, 1989; *Marone and Kilgore*, 1993], triaxial sawcut [*Engelder et al.*, 1975; *Summers and Byerlee*, 1977; *Byerlee et al.*, 1978; *Logan et al.*, 1979; *Shimamoto and Logan*, 1981; *Marone et al.*, 1990], and rotary shear [*Mandl et al.*, 1977; *Tullis et al.*, 1989].

Much of this work has focused on understanding the time dependence and rate dependence of friction. The associated variations in friction are small (1–2%, if the sliding rate changes by an order of magnitude), but they control the stability of frictional slip and hence the seismic potential of faults. Here, our focus is on variations in the basic, rate-independent frictional strength of gouge layers. The strength variations we discuss are independent of those due to variations in pore fluid pressure [e.g., *Byerlee*, 1990; *Rice*, 1992].

---

[1] Now at Department of Geological Sciences, University College London.

The following phenomena are discussed in many of the studies listed above and are of particular interest in this study.

1. The frictional strength of a gouge layer depends on its thickness, the grain size distribution, and to a lesser extent on the roughness of the solid surfaces that confine the layer [e.g., *Dieterich*, 1981].

2. Grain fragmentation is an active process in gouge deformation and results in a power law distribution of grain size regardless of the initial state [e.g., *Biegel et al.*, 1989].

3. Oblique Riedel shears are ubiquitous in sheared layers after moderate amounts of strain [e.g., *Logan et al.*, 1979].

4. During shear, the orientation of stress in a gouge layer (either measured or inferred from the microstructure) evolves to bring the maximum compressive stress to an angle of 45° to the layer, regardless of the orientation of stress outside the layer [e.g., *Mandl*, 1977].

In this study we present observations and analysis that reveal the mechanics linking these phenomena. Detailed observations of the thinning of gouge layers during double-direct-shear experiments show a strong correlation between the amount of layer thinning and the frictional strength. This behavior is analyzed using rate-independent Mohr-Coulomb plasticity, extending an approach suggested by *Byerlee and Savage* [1992]. The observations are found to be consistent with a constant coefficient of internal friction for quartz gouge in plane strain.

Experiments

We carried out experiments in a double-direct-shear apparatus, described in detail by *Dieterich* [1981] and by *Linker and Dieterich* [1992]. In this geometry, a pair of identical gouge layers are sandwiched between three solid sample blocks (see Figure 1). This assembly is compressed laterally by a servo-controlled hydraulic ram, maintaining a constant normal stress on the gouge layers. The central sample block is then forced down between the gouge layers by a second servo-controlled ram, while the side sample blocks are restrained from moving vertically. The motion of the central sample block is resisted only by the gouge layers and the experiment therefore provides an accurate measurement of the frictional strength of the gouge layers.

The exposed edges of the gouge layers are unconfined, and gouge could in principle escape up, down, or laterally. In practice, most of the gouge lost from a layer is carried beyond the lower edge of the side sample blocks by the larger central sample block, as sketched in Figure 1. This observation is significant in the analysis of these experiments, because it indicates that the gouge is deforming in plane strain.

Table 1 lists the experimental conditions used in 23 experiments. Results from some of these experiments have already been reported by *Marone and Kilgore* [1993], who discuss aspects of the rate dependence of friction in gouge layers.
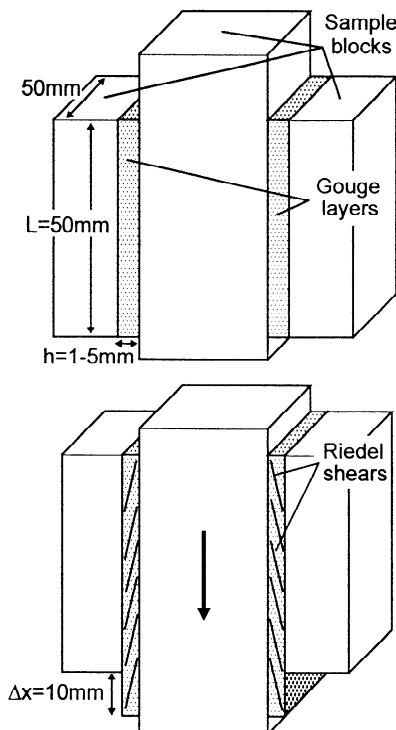

Figure 1. Schematic diagram of the double-direct-shear experimental geometry, showing the sample assembly before and after an experiment.

Sample Preparation

Gouge. Mosts of the experiments reported here were performed using simulated gouge consisting of Ottawa sand, a pure (>99.9%) quartz sand available commercially from U.S. Silica Company, Ottawa, Illinois.

Table 1. Experimental Conditions

Experiment	Gouge Type	h, mm	Sample Blocks (Roughness)
u01	coarse	3	Westerley (50 μm)
u04	coarse	3	Westerley (0.2 μm)
u08	coarse	3	grooved steel
u09	coarse	6	grooved steel
u10	coarse	1	grooved steel
u11	coarse	6	Westerley (0.2 μm)
u23	coarse	6	grooved steel
u26	coarse	3	grooved steel
u27	coarse	10	grooved steel
u29	coarse	1	grooved steel
u02	medium	3	Westerley (0.2 μm)
u03	medium	3	Westerley (50 μm)
u07	ultrafine	1	Westerley (50 μm)
u12	ultrafine	1	grooved steel
u13	ultrafine	3	grooved steel
u14	ultrafine	6	grooved steel
u22	ultrafine	3	grooved steel
u15	fractal	6	grooved steel
u16	fractal	3	grooved steel
u17	fractal	1	grooved steel
u31	Lopez	3	grooved steel
u32	Lopez	6	grooved steel
u33	Lopez	1	grooved steel

Four different initial grain size distributions were used: (1) coarse gouge (ASTM C-190), containing well-sorted grains with diameters in the range of 400-800 μm, (2) medium gouge, prepared by crushing and sieving the coarse gouge to leave grains with a range of diameters below 106 μm, (3) ultrafine gouge (Silcosil #400 mesh), with median and maximum grain diameters of 1.4 μm and 10 μm, respectively [see *Marone and Kilgore*, 1993], and (4) fractal gouge, intended to simulate the power law grain size distribution found in natural fault gouge [*Sammis et al.*, 1987; *Sammis and Biegel*, 1989]. Crushed sand was sieved into size fractions each having a size range of approximately a factor of 2: <45 μm, 45-90 μm, 90-175 μm, 175-350 μm and 350-710 μm. These fractions were then remixed in measured proportions to produce a power law grain size distribution (see *Biegel et al.* [1989] for details).

A few experiments were performed using natural gouge from the Lopez fault in the San Gabriel fault zone, California. A site description is given by *Sammis et al.* [1987]. The Lopez gouge is mostly quartz, with minor albite and 5-10% smectite [*Scott et al.* 1994]. *Sammis et al.* [1987] and *Sammis and Biegel* [1989] measured grain sizes in Lopez gouge and found that there is a power law distribution over the size range of 5-1000 μm.

The grain size distribution of the gouge layers evolves during the experiments due to grain fragmentation. In particular, the coarse gouge was quickly crushed to produce finer grains.

Sample blocks. Most of the experiments were performed using grooved steel sample blocks (see Table 1). The surfaces of the steel facing the gouge layers were roughened by a regular array of square grooves 250 μm wide, 500 μm deep, and spaced 250 μm apart. The grooves were oriented perpendicular to the direction of shearing.

A few experiments were performed using Westerley granite sample blocks with different surface roughnesses, including some with very smooth surfaces (#600 grit polish, 0.2 μm rms surface roughness).

Initial layer thickness. The gouge layers were prepared, using a jig, to give an initial thickness of between 1 and 10 mm at room pressure (see Table 1). The thinnest layers of coarse gouge were initially a monolayer of grains separating the sample blocks. The initial thicknesses of the two layers in an individual experiment differed by no more than 5%. All the gouge layers were initially 50 mm in length and width, matching the dimensions of the smaller side sample blocks.

After the total thickness of the assembly on the bench was measured, the assembly was inserted into the load frame and a small normal load was applied. From this point, relative changes in the combined thickness of the two layers were measured with a displacement transducer (DC-LVDT). Note that the layer thickness data presented below were measured at a normal stress of 25 MPa and are therefore smaller than the initial thicknesses, even before shearing.

Typical Results

During each experiment the applied normal and shear stresses, layer thickness, and shear displacement were continuously recorded by a microcomputer. The stresses were measured using conventional load cells. The shear displacement was measured with a displacement transducer and later corrected for elastic distortion of the experimental apparatus. In all the experiments, the normal stress was held constant at 25 MPa by servo control. The shear displacement rate was also servo-controlled. Typical results for a single experiment are shown in Figure 2.
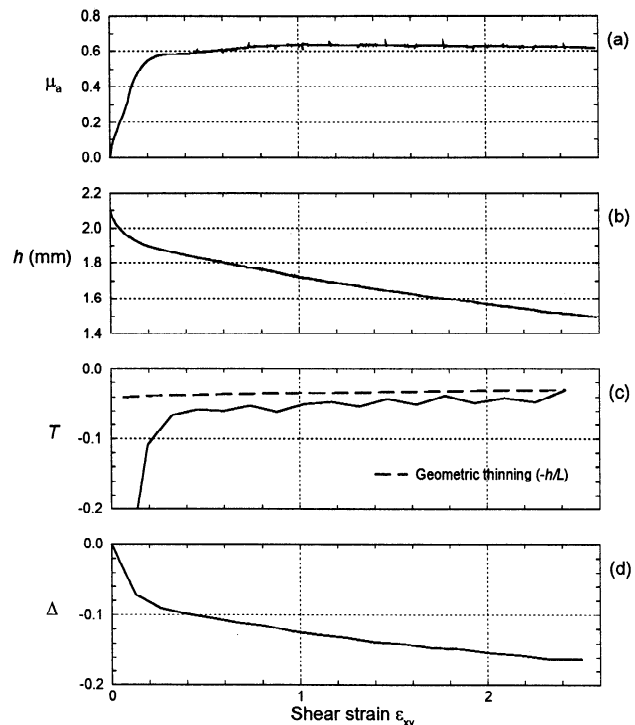

Figure 2. Results from a single experiment (u16) that used simulated quartz gouge with a fractal grain size distribution, and rough steel sample blocks. All the quantities are shown plotted against shear strain, which was calculated by integrating $\delta X/2h$, using equation (1). The total shear displacement X was 10 mm. (a) Apparent friction μ_a, defined as the ratio of the applied shear and normal stresses. The small fluctuations in the latter part of the experiment are associated with changes in the sliding velocity. (b) Thickness h of one layer. This layer was 3 mm thick at room pressure and 2.1 mm thick under a normal stress of 25 MPa at the initiation of shear displacement. (c) Rate of change of layer thickness with respect to shear displacement (the thinning ratio) $T = dh/dX$, as a solid line. This derivative is calculated over increments of 0.5 mm in shear displacement in order to provide some smoothing. The dashed line is the predicted rate of "geometric thinning" due to extrusion T_{GT}, from equation (42). (d) Volumetric strain, estimated from the difference between the observed and "geometric" rates of thinning, using equation (49).

Shear strain. The data shown are plotted against shear strain rather than shear displacement; the shear strain ϵ_{xy} is defined as follows:

$$\epsilon_{xy} = \int \frac{dX}{2h} \tag{1}$$

where X is the shear displacement, and h is the layer thickness. The coordinates x and y are parallel and perpendicular to the layer, respectively (see Figure 3a). In the example shown in Figure 2, the final shear displacement was 10 mm and the average layer thickness was 2 mm, so the final shear strain was around 2.5.

Apparent friction. The apparent friction μ_a of a layer is defined as the ratio of the applied shear stress σ_{xy} and normal stress σ_{yy}:

Figure 3. Stress and strain in a sheared layer. The shaded regions represent the solid sample blocks, surrounding an unshaded gouge layer. (a) Coordinate system and applied stresses; the σ_{yy} and σ_{xy} components of stress are measured, but the σ_{xx} component is not. (b) Principal stresses; the angle θ is 45° for a layer of constant thickness and is smaller for a layer that is thinning (see equations (17) and (38)). (c) Slip planes showing the sense of displacement. The low-angle slip planes are presumed to correspond to the Reidel shears sketched in Figure 1.

$$\mu_a = \frac{\sigma_{xy}}{|\sigma_{yy}|} \, . \tag{2}$$

The applied stresses are shown in Figure 3a. It is assumed that these stresses are uniform across both layers and across the entire area of each layer.

The apparent friction of the layers initially rises rapidly (see Figure 2a). By the time the shear strain has reached about 0.3, the apparent friction has reached a steady level, although some slow evolution is observed during the remainder of the experiment.

Thinning ratio. The rate of change of layer thickness is quantified by the thinning ratio T, which is defined as the rate of change in layer thickness h with respect to shear displacement X:

$$T = \frac{dh}{dX} \, . \tag{3}$$

It is assumed that both layers thin at the same rate.

During the transient rise in apparent friction the layers thin rapidly, by about 10% of their initial thickness (see Figure 2b). After the initial transient, the layer thickness decreases more slowly, but layer thinning continues at a steady rate.

This observation is crucial; the continuing thinning demonstrates unambiguously that strain is distributed throughout the gouge layers. If strain were confined, for example, to the boundary between the gouge layers and the sample blocks, the steady thinning of the layers would not occur. The observation of layer thinning is the foundation of the analysis presented below.

Summary of Results

Figure 4 shows a summary of results from all the experiments listed in Table 1. Each experiment is represented by a single symbol in each plot. A representative point was chosen from the latter, steady state part of each experiment, and the apparent friction, thinning ratio, and instantaneous layer thickness were recorded. These data are presented as plots of the apparent friction versus thinning ratio (Figure 4a) and the layer thickness versus thinning ratio (Figure 4b). In Figure 4b, the layer thickness is scaled by the length of the side sample blocks L, which is 50 mm in all the experiments (see Figure 1).

Figure 4a shows a large range in apparent friction and a clear negative correlation between the apparent friction and the thinning ratio. There are no major departures from this trend as a function of the gouge type, although the lowest values of apparent friction are all for coarse gouge. The types of sample block are not shown in Figure 4, but no significant variations were found as a function of the type or roughness of the sample blocks. For example, experiments u02 and u03 gave almost identical results; both used 3 mm layers of medium gouge, but the Westerley sample blocks were rough in one case and very smooth in the other (see Table 1).

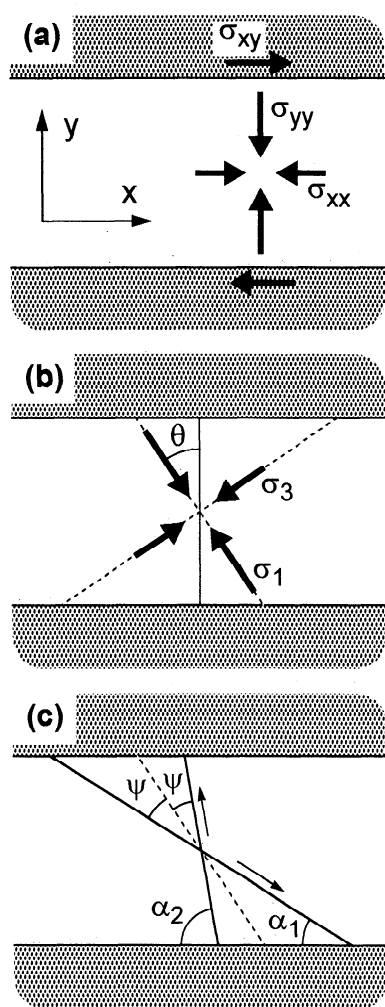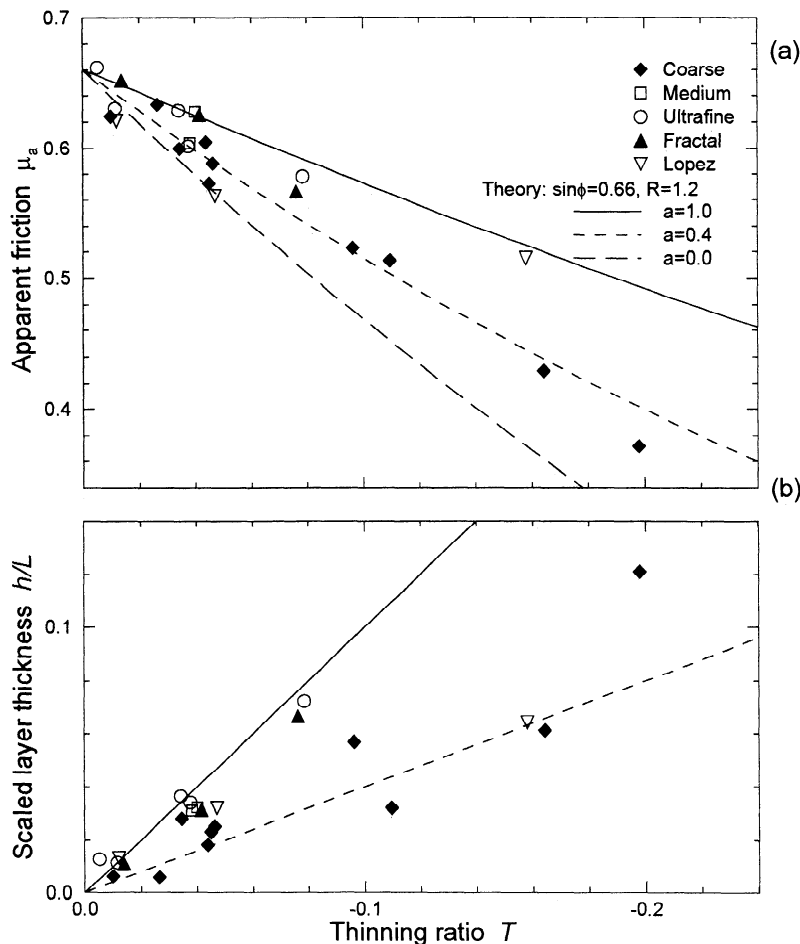Figure 4b shows that the higher thinning ratios are associated with thicker layers. Also, at a given layer

Figure 4. Summary of results from all the experiments, showing their fit to the theory presented in the text for (a) apparent friction μ_a and (b) scaled layer thickness h/L, both as a function of the thinning ratio T. In both plots, the symbols show the data and the lines show the theory. The legend indicates the types of gouge corresponding to the different symbols. Theoretical predictions are shown for different values of the variable a: the lines in Figure 4a represent equation (41), and the lines in Figure 4b represent equation (45). Layer thinning is attributed entirely to extrusion when $a = 1$, and entirely to densification when $a = 0$. An intermediate case ($a = 0.4$) is also shown on both plots; the region between $a = 1$ and $a = 0.4$ encompasses most of the data in both plots.

thickness, the coarse gouge shows a higher thinning ratio than do the other types.

Analysis

The goal of this analysis is to account for the trends in apparent friction and layer thinning shown in Figure 4. This is accomplished by considering the two mechanisms that could be responsible for layer thinning: (1) extrusion of gouge from the center out to the unconfined edges of the layer and (2) densification of the gouge by grain rearrangement and fragmentation. The analysis is developed in two stages. First, we assume that the gouge density remains constant so that all the thinning is attributed to extrusion. Second, densification of the gouge is permitted providing an additional mechanism for layer thinning.

The geometry used for this analysis is shown in Figure 3a. A Cartesian coordinate system (x, y, z) is used such

that x is parallel to both the layer and the direction of shearing, y is perpendicular to the layer, and z is parallel to the layer and perpendicular to the direction of shearing. The layer has thickness h in the y direction and length L in the x direction (see Figure 1). We follow the convention that compressive stresses are negative.

Thinning due to Extrusion at Constant Density

In this section, the density of the gouge is assumed to remain constant during shear deformation. Plane strain is also assumed, so that variations in the z direction are not considered. The final assumption is that the plastic strain rate tensor is directly proportional to the deviatoric stress, which is the coaxiality assumption commonly made in plasticity [Hill, 1960].

Plastic strain. An increment δX of shear displacement drives a change in layer thickness δh. The following components of the incremental plastic strain tensor can therefore be obtained directly:

$$\delta\epsilon_{yy} = \frac{\delta h}{h} \; ; \tag{4}$$

$$\delta\epsilon_{xy} = \frac{\delta X}{2h} \; . \tag{5}$$

Because the density is constant and strain is confined to the x–y plane, the increment of extensional strain within the layer $\delta\epsilon_{xx}$ is equal and opposite to $\delta\epsilon_{yy}$. By dividing the strain increments by an arbitrary time increment, the strain rate tensor can be written as follows:

$$\dot{\epsilon}_{ij} = \dot{\epsilon}_{xy} \begin{bmatrix} -2T & 1 \\ 1 & 2T \end{bmatrix} \tag{6}$$

where the thinning ratio T is, as before, the rate of thinning of the layer with respect to shear displacement:

$$T = \frac{dh}{dX} = \frac{\delta\epsilon_{yy}}{2\delta\epsilon_{xy}} \; . \tag{7}$$

Note that T is negative when the layer is thinning. All the quantities in the expression for the strain rate tensor (6) are known.

Stress. The σ_{yy} and σ_{xy} components of stress are measured directly. The σ_{xx} component of stress is not measured, but it can be estimated by using a relationship between the stress and strain rate tensors. First, it is convenient to decompose the stress tensor into its isotropic and deviatoric parts:

$$\sigma_{ij} = \bar{\sigma}\delta_{ij} + \sigma'_{ij} \tag{8}$$

where δ_{ij} is the Kronecker delta. The mean stress $\bar{\sigma}$ is given by

$$\bar{\sigma} = \tfrac{1}{2}(\sigma_{xx} + \sigma_{yy}) \tag{9}$$

and the trace of the deviatoric stress tensor σ'_{ij} is zero.

This analysis now hinges on the assumption that the deviatoric stress tensor in equation (8) is coaxial with the strain rate tensor in equation (6), which can be simply stated as follows:

$$\sigma'_{ij} = m\dot{\epsilon}_{ij} \tag{10}$$

where m is an unknown scalar modulus that can vary (e.g., with the total shear strain). Using equation (10), the deviatoric stress can be written using the same tensorial form used for the strain rate in equation (6):

$$\sigma'_{ij} = \sigma_{xy} \begin{bmatrix} -2T & 1 \\ 1 & 2T \end{bmatrix} \; . \tag{11}$$

By comparing the xx and yy components of this equation, the unknown σ_{xx} component of stress can be constrained:

$$\sigma_{yy} - \sigma_{xx} = 4T\sigma_{xy} \; . \tag{12}$$

The entire stress tensor is now determined.

Figure 5 shows a Mohr's circle diagram representing this state of stress. The center of the stress circle is given by the mean stress $\bar{\sigma}$; from equations (9) and (12), $\bar{\sigma}$ can be written explicitly as follows:
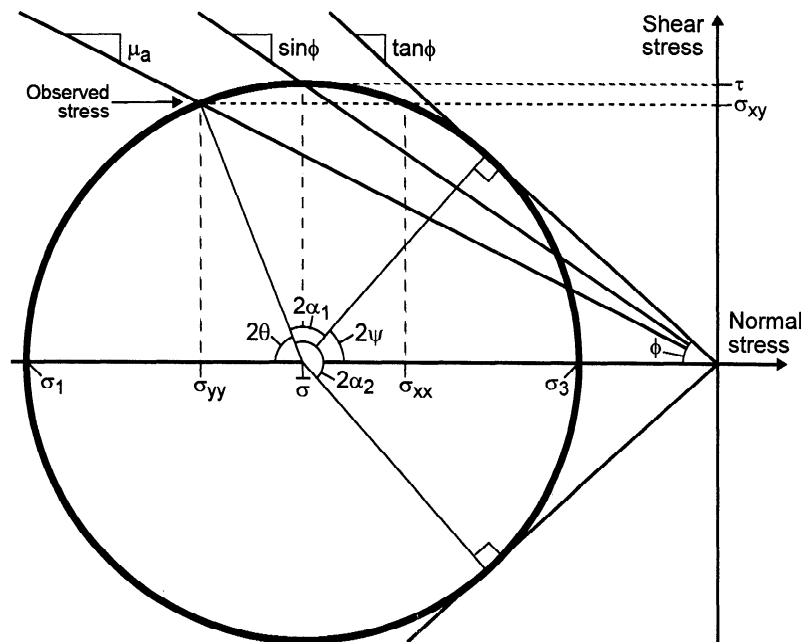
$$\bar{\sigma} = \sigma_{yy} - 2T\sigma_{xy} \; . \tag{13}$$

Figure 5. Mohr diagram showing the state of stress in a sheared layer that is thinning by extrusion. The observed stresses (σ_{yy} and σ_{xy}) alone do not constrain the Mohr circle, but the observed strain can be used to estimate the σ_{xx} component of stress and hence to determine the stress circle. The apparent friction μ_a obtained directly from the observed stresses is significantly smaller than the internal friction of the gouge, parameterized by $\tan\phi$. In the limit of a layer that does not thin, the observed stress lies at the apex of the circle; in this case, $\sigma_{xx} = \sigma_{yy}$ and $\mu_a = \sin\phi$. The angles in this diagram and Figure 3 are correctly scaled for $\sin\phi = 0.66$ and $T = -0.2$.

Note that since σ_{yy} and $\bar{\sigma}$ are negative,

$$|\bar{\sigma}| = |\sigma_{yy}| + 2T\sigma_{xy} . \tag{14}$$

The radius of the stress circle τ is an objective measure of the shear stress in the x–y plane and is defined by:

$$\tau^2 = \sigma_{xy}^2 + \left(\frac{\sigma_{yy} - \sigma_{xx}}{2}\right)^2 . \tag{15}$$

Using equation (12),

$$\tau = \sigma_{xy}\sqrt{1 + 4T^2} . \tag{16}$$

The magnitudes of the principal stresses (σ_1 and σ_3) are $\bar{\sigma} \pm \tau$. In Figure 5, the principal stresses lie at the intersection of the stress circle with the horizontal axis. The orientation of the principal stresses is represented by the angle θ between the maximum compressive stress and the y direction, which is also shown in Figure 5. This angle can be obtained using equation (13) and the Mohr diagram:

$$\tan 2\theta = \frac{\sigma_{xy}}{|\sigma_{yy} - \bar{\sigma}|} = \frac{1}{2|T|} . \tag{17}$$

The orientation of the principal stress axes in the layer is shown in Figure 3b. Note that when $T = 0$, $\sigma_{xx} = \sigma_{yy} = \bar{\sigma}$ and $\sigma_{xy} = \tau$. In this case the principal axes of stress lie at 45° to the layer; this result was observed directly by *Mandl et al.* [1977] in experiments on granular layers at low stress levels. Figure 3b and Figure 5 illustrate a case where $T < 0$, $|\sigma_{yy}| > |\bar{\sigma}| > |\sigma_{xx}|$ and $\sigma_{xy} < \tau$. In such cases the direction of maximum compressive stress moves closer to the y direction, driving the layer thinning.

Slip planes and internal friction. According to standard Mohr-Coulomb plasticity, the strain that accompanies this state of stress is accommodated by displacement on sets of conjugate slip planes. As shown in Figure 3c, these slip planes are positioned symmetrically about the direction of maximum compressive stress, at angles $\pm\psi$. *Byerlee and Savage* [1992] note that for the case of plane strain in an incompressible material, slip on two sets of distinct planes can be combined to give any macroscopic strain tensor.

The orientations of these slip planes are such that the ratio of shear stress to normal stress acting on them is at a maximum. This ratio, μ, is an objective measure of the intrinsic, or internal, frictional strength of the gouge. The internal friction is conveniently parameterized by the angle of friction ϕ, where $\mu = \tan\phi$.

On the Mohr diagram (Figure 5) lines are shown at angles $\pm\phi$ to the horizontal axis that are tangent to the stress circle. These lines represent the Mohr-Coulomb failure envelope for plastic shear deformation; states of stress outside these lines are not accessible. Note that we assume that the cohesion of the gouge is negligible. The slope of the failure envelope μ is given by

$$\mu = \tan\phi = \frac{\tau}{\sqrt{\bar{\sigma}^2 - \tau^2}} . \tag{18}$$

As shown in Figure 5, the angle of the slip planes ψ is related to the angle of friction ϕ by

$$2\psi = \frac{\pi}{2} - \phi \quad \Rightarrow \quad \cos 2\psi = \frac{\tau}{|\bar{\sigma}|} . \tag{19}$$

If we note that the orientation of the maximum compressive stress is given by θ, the angles of the slip planes from the x direction, α_1 and α_2, can be given by

$$\alpha_1 = \frac{\pi}{2} - \theta - \psi ; \tag{20}$$

$$\alpha_2 = \frac{\pi}{2} - \theta + \psi . \tag{21}$$

These angles are shown in Figure 3c and Figure 5.

The shear planes defined by the angles α_1 and α_2 are referred to as Riedel shears. When the double-direct-shear samples are disassembled, the low-angle (α_1) Riedel shears can be seen as planes along which the gouge preferentially parts (see Figure 1).

Apparent friction. It has been noted previously that the apparent friction of a gouge layer, as defined by equation (2), is always less than the internal friction μ of the gouge. In fact, the apparent friction is the sine of the angle of friction ϕ rather than its tangent. This inference is implicit in a discussion by *Logan et al.* [1979] and has been stated explicitly by *Hobbs et al.* [1990] and *Marone et al.* [1992]. *Byerlee and Savage* [1992] discuss the matter in more detail; their analysis represents the limit where $T = 0$ and $\theta = 45°$, in which case the apparent friction is simply the ratio of the shear stress and mean stress:

$$\mu_a = \frac{\tau}{|\bar{\sigma}|} = \sin\phi . \tag{22}$$

A line with this slope is shown in Figure 5; it runs through the apex of the stress circle.

For cases where $T < 0$, we can obtain a relationship between the apparent friction μ_a and the thinning ratio T by first using equations (14) and (16) to obtain the ratio of the shear and mean stresses:

$$\frac{\tau}{|\bar{\sigma}|} = \sin\phi = \frac{\sigma_{xy}\sqrt{1 + 4T^2}}{|\sigma_{yy}| + 2T\sigma_{xy}} . \tag{23}$$

Noting the definition of apparent friction (2) and rearranging, we obtain:

$$\mu_a = \frac{\sin\phi}{\sqrt{1 + 4T^2} - 2T\sin\phi} . \tag{24}$$

A line with this slope is shown on the Mohr diagram for $T < 0$, $\mu_a < \sin\phi$; it intersects the stress circle at a normal stress σ_{yy} and a shear stress σ_{xy}.

The expression (24) contains only one adjustable material parameter, $\sin\phi$, which is directly related to the internal friction $\mu = \tan\phi$ and should therefore be constant for a given material. For example, if $\mu = 0.88$ ($\phi = 41.3°$) the predicted apparent friction when $T = 0$ is $\mu_a = 0.66$. When $T = -0.1$, the predicted apparent friction drops to $\mu_a = 0.57$. In this case, equation (17) gives $\theta = 39.3°$, equation (19) gives $\psi = 24.4°$, and

equations (20) and (21) give $\alpha_1 = 26.3°$ and $\alpha_2 = 75.1°$, respectively.

Comparison with observations. This simple theory goes a long way toward explaining the observed anomalies in apparent friction as a function of the observed layer thinning. The solid line in Figure 4a shows the apparent friction predicted by equation (24) with $\sin \phi = 0.66$ and provides an upper bound to all the observations. If some random scatter were accepted, a slightly smaller value for $\sin \phi$ would fit most of the data out to $T \sim -0.1$. However, as the thinning ratio becomes large, the theory clearly predicts systematically greater values for apparent friction than are observed. As is shown below, a further reduction in the apparent friction is predicted when densification of the layer is occurring.

Thinning due to Extrusion and Densification

In this section we augment the theory presented above, to assess the effect of gouge densification on the apparent friction. The approach to this analysis is similar to that used for the constant density case

1. Construct a strain rate tensor that admits changes in volume, but retain the assumption of plane strain in the x–y plane.

2. Construct a stress tensor, again assuming that the stress and strain rate tensors are coaxial.

3. Use a flow law to relate the volumetric strain rate to the shear strain rate and the state of stress.

Plastic strain. As before, the $\dot{\epsilon}_{yy}$ and $\dot{\epsilon}_{xy}$ components of the plastic strain rate tensor are known. In plane strain, only the $\dot{\epsilon}_{xx}$ component is unknown, representing longitudinal strain in the layer. Figure 6 shows a decomposition of the incremental strain into components of shear, extrusion, and densification. A strain rate tensor with these components may be written as follows:

$$\dot{\epsilon}_{ij} = \dot{\epsilon}_{xy} \begin{bmatrix} 0 & 1 & 0 \\ 1 & 0 & 0 \\ 0 & 0 & 0 \end{bmatrix} + \dot{\epsilon}_{xy} \begin{bmatrix} -2Ta & 0 & 0 \\ 0 & 2Ta & 0 \\ 0 & 0 & 0 \end{bmatrix}$$

$$+ \dot{\epsilon}_{xy} \begin{bmatrix} 0 & 0 & 0 \\ 0 & 2T(1-a) & 0 \\ 0 & 0 & 0 \end{bmatrix} \qquad (25)$$

where the three terms on the right-hand side describe shear, extrusion, and densification, respectively. T is again the thinning ratio dh/dX and is negative. The variable a determines the distribution of the observed thinning between extrusion and densification. When $a = 1$, the density is constant and the thinning is attributed entirely to extrusion. When $a = 0$, there is no extrusion ($\dot{\epsilon}_{xx} = 0$), and the thinning is due entirely to densification.

The form of the extrusion term in equation (25) implies anisotropy in the behavior of the layer parallel and perpendicular to the direction of shearing, that is, extrusion is assumed to occur in the x direction but not in the z direction. It might be expected that once plastic strain had been mobilized by application of the shear

stress σ_{xy}, the extrusion component of strain might occur in both x and z directions. Similarly, the form of the densification term in equation (25) assumes uniaxial compression across the layer rather than isotropic compression. These assumptions are adopted because they produce plane strain regardless of the value of a, consistent with the experimental observation that relatively little gouge is driven out from the layers perpendicular to the direction of shearing (see Figure 1).

The terms in equation (25) may be combined to give:

$$\dot{\epsilon}_{ij} = \dot{\epsilon}_{xy} \begin{bmatrix} -2Ta & 1 & 0 \\ 1 & 2T & 0 \\ 0 & 0 & 0 \end{bmatrix} . \qquad (26)$$

We now separate the strain rate into its isotropic and deviatoric parts:

$$\dot{\epsilon}_{ij} = \frac{1}{3}\dot{\Delta}\delta_{ij} + \dot{\epsilon}_{xy}D_{ij} . \qquad (27)$$

The volumetric strain rate $\dot{\Delta}$ is given by

$$\dot{\Delta} = 2T(1-a)\dot{\epsilon}_{xy} . \qquad (28)$$

The nondimensional tensor D_{ij} describes the geometry of the deviatoric strain rate:

$$D_{ij} = \begin{bmatrix} -\frac{2T(1+2a)}{3} & 1 & 0 \\ 1 & \frac{2T(2+a)}{3} & 0 \\ 0 & 0 & -\frac{2T(1-a)}{3} \end{bmatrix} . \qquad (29)$$

The nonzero zz component of this tensor arises solely from the assumption of plane strain during densification.

An objective measure $\dot{\gamma}$ of the shear strain rate in the x–y plane is defined using a similar form to that used for the shear stress τ in equation (15):

$$\dot{\gamma}^2 = \dot{\epsilon}_{xy}^2 + \left(\frac{\dot{\epsilon}_{yy} - \dot{\epsilon}_{xx}}{2}\right)^2 . \qquad (30)$$

Expanding this expression using equation (26) gives

$$\dot{\gamma} = F\dot{\epsilon}_{xy} \qquad (31)$$

where

$$F = \sqrt{1 + T^2(1+a)^2} . \qquad (32)$$

Stress. Our knowledge of the stress tensor is, like the strain rate tensor, limited to the σ_{yy} and σ_{xy} components; we do not have a direct measurement of σ_{xx}. We again adopt the coaxiality assumption of plasticity, so that the deviatoric stress tensor is coaxial with the deviatoric strain rate:

$$\sigma'_{ij} = \sigma_{xy}D_{ij} . \qquad (33)$$

Equations (29) and (33) imply that the σ'_{zz} is nonzero when densification is occurring ($a < 1$). This arises from assumptions of coaxiality and plane strain. The zz component of stress (which is the intermediate principal stress σ_2) is implicitly assumed to adjust to a value

between σ_{xx} and σ_{yy} (or σ_1 and σ_3), as necessary to maintain plane strain.

From equation (29), the xx and yy components of equation (33) give

$$\sigma_{yy} - \sigma_{xx} = 2T(1 + a)\sigma_{xy} . \tag{34}$$

We now construct expressions for the mean stress and shear stress in the x–y plane. The mean stress in the x–y plane $\bar{\sigma}$ is again defined by equation (9); using equation (34), we obtain

$$\sigma = \sigma_{yy} - T(1 + a)\sigma_{xy} \tag{35}$$

and, since σ_{yy} and $\bar{\sigma}$ are negative,

$$|\bar{\sigma}| = |\sigma_{yy}| + T(1 + a)\sigma_{xy} . \tag{36}$$

As before, the shear stress in quantified by the radius τ of the Mohr circle in the x–y plane. Using equations (15) and (34), we obtain

$$\tau = F\sigma_{xy} \tag{37}$$

where F is again given by equation (32).

As in equation (17), the orientation of the principal stresses can be obtained from equation (35) and is shown to depend on the rate of densification through the variable a:

$$\tan 2\theta = \frac{1}{(1 + a)|T|} . \tag{38}$$

Flow law. At this point there is only one unknown in the problem: the variable a that determines the relative amounts of compaction and extrusion. The constant volume theory can be recovered by setting $a = 1$. To treat cases where $a < 1$, some relationship between the volumetric and shear strain rates must be introduced. The flow law used here is as follows:

$$\dot{\Delta} = R \left(\frac{\tau}{|\bar{\sigma}|} - \sin \phi \right) \dot{\gamma} \tag{39}$$

where R is a dimensionless flow constant (we later suggest that R is around unity). This flow law has the property that the volume change vanishes as the Mohr-Coulomb condition $\tau/|\bar{\sigma}| = \sin \phi$ is reached. If the volume strain is negative (densification), $\tau/|\bar{\sigma}| < \sin \phi$. In effect, the gouge has a reduced internal friction during densification. Similar flow laws are used in critical state soil mechanics [Britto and Gunn, 1987]. The term "critical state" refers to the final state of constant-density deformation.

Note that the Mohr-Coulomb failure condition depends on the maximum and minimum principal stresses (in the x–y plane) but not on the intermediate principal stress (in the z direction). Consequently, the quantities τ and $\bar{\sigma}$ in equation (39) are defined by equations (15) and (9) in terms of only the σ_{xx}, σ_{yy}, and σ_{xy} components of stress. In granular soils the intermediate principal stress affects the failure strength [Green and Bishop, 1969; Mandl, 1988]. The coefficient of internal

friction obtained from plane-strain experiments such as ours is expected to overestimate the strength of a sample in triaxial compression.

Substituting from equations (28), (31), (36), and (37) into the flow law (39), we obtain

$$\frac{2T(1 - a)}{RF} = \frac{F\mu_a}{1 + T(1 + a)\mu_a} - \sin \phi \tag{40}$$

where the apparent friction μ_a is defined by equation (2). With some rearrangement, the apparent friction is given by

$$\mu_a = \frac{RF\sin \phi + 2T(1 - a)}{RF^2 - T(1 + a)[RF\sin \phi + 2T(1 - a)]} . \tag{41}$$

The apparent friction μ_a and thinning T are the observed, independent variables in this expression. There are two adjustable material parameters: $\sin \phi$ and R. The quantity F is defined in terms of T and a by equation (32), but the variable a remains independent and is not directly observed. Below, we show that a can be estimated by further examination of the data.

In the limit where $a = 1$, equation (24) for thinning at constant density is recovered. The flow law constant R does not appear in this limiting case. The behavior in this limit may be used to estimate the material parameter $\sin \phi$ and hence the internal friction μ of the gouge.

With densification included in the analysis, gouge with a constant internal friction of $\mu = 0.88$ may display a wider range of values for apparent friction. At a constant thinning ratio of $T = -0.1$ the apparent friction ranges between $\mu_a = 0.57$ when $a = 1$ (extrusion only) and $\mu_a = 0.47$ when $R = 1.2$ and $a = 0$ (densification only). Under the same conditions, the orientation of the stress tensor changes from $\theta = 39.3°$ to $\theta = 42.1°$ (see equation (38)).

Geometric thinning. Inspection of the layers during and after the experiments shows that a band of gouge of comparable thickness to the layer is left behind on the larger sample block (see Figure 1). At the leading edge of the smaller sample block, the gouge neither extrudes out ahead of the edge nor falls behind to leave a gap containing no gouge. This observation suggests a process of "geometric thinning" (GT) in which, when the layer advances a distance δX, a volume of gouge $h\delta X$ is left behind at the trailing edge of the smaller sample blocks. A component δh_{GT} of the incremental thinning of the layer exactly balances this loss:

$$h\delta X = -L\delta h_{GT} \quad \Rightarrow \quad \frac{dh}{dX}\bigg|_{GT} = -\frac{h}{L} = T_{GT} \tag{42}$$

where L is the length of the side sample blocks. Equation (42) links the contribution of extrusion to layer thinning to the overall dimensions of the layer. The idea of GT can be exploited to produce an estimate of the variable a, in cases where the observed thinning ratio T is larger than T_{GT}.

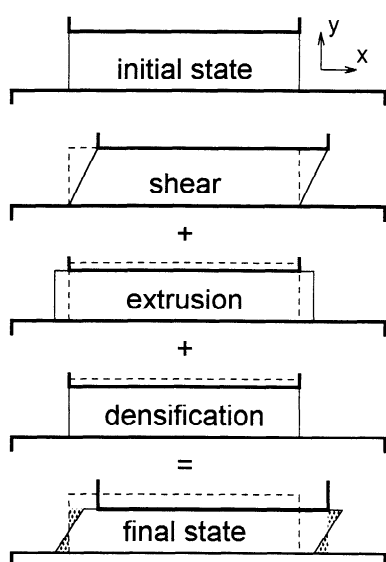First, consider the unique relationship between the

Figure 6. Decomposition of strain in a sheared layer that thins by extrusion and densification. The heavier lines in each diagram show the sample blocks. The initial shape of the layer, shown in the upper diagram, is repeated as a dashed outline in the other diagrams for reference. In this illustration, the thinning of the layer in the final state is attributed to equal amount of extrusion and densification ($a = 0.5$). The relative amounts of shear and extrusion are correctly scaled to reproduce the condition of "geometric thinning," in which the advance of the right-hand edge of the gouge layer matches the advance of the smaller (upper) sample block. It is assumed that the local transport of gouge between the shaded triangles conserves the rectilinear shape of the layer, particularly at the right-hand edge.

shear and extrusion components of strain illustrated in Figure 6. The $\dot{\epsilon}_{xx}$ component of strain rate has adjusted so that the right-hand edge of the layer advances with the smaller sample block while the left-hand edge remains in place on the larger sample block. The required increment in extensional strain is given by

$$\delta\epsilon_{xx} = \frac{\delta X}{L} . \tag{43}$$

Note that the magnitude of $\dot{\epsilon}_{xx}$ is independent of rate of densification, which contributes only to $\dot{\epsilon}_{yy}$ (see equation (25)).

Second, an expression for $\delta\epsilon_{xx}$ involving the variables a and T may be obtained from equations (5) and (26):

$$\delta\epsilon_{xx} = -2Ta\delta\epsilon_{xy} = -\frac{Ta\delta X}{h} . \tag{44}$$

Equating (43) and (44) eliminates δX to give

$$a = -\frac{h}{LT} . \tag{45}$$

Comparing equations (42) and (45) confirms that when thinning is due to extrusion alone ($a = 1$), T is equal to T_{GT}. Equation (45) can be used to estimate a, thereby

leaving only the material parameters $\sin\phi$ and R as unknowns in equation (41).

Comparision with observations. There is good quantitative evidence to support the idea that the rate of extrusion is determined by GT.

1. Figure 2c shows a comparison of T_{GT} from equation (42) and the observed thinning ratio during a single experiment; the observed rate steadily converges towards T_{GT} as the shear strain increases.

2. Figure 4b shows the final thinning ratio plotted against the scaled layer thickness h/L for all the experiments. Two theoretical lines representing equation (45) are also shown, for $a = 1$ and $a = 0.4$. The line $a = 1$ corresponds to constant gouge density and $T = T_{GT}$. With the exception of one very thin layer, the (absolute) thinning ratio is never smaller than T_{GT}. The one exception is a very thin layer between sample blocks of significant roughness, which makes a precise definition of the layer thickness problematic.

By using the the additional constraint provided by GT, the observations of apparent friction can be used to estimate the material parameter R. In Figure 4a, equation (41) is plotted for $a = 0, 0.4,$ and 1. A value of $\sin\phi = 0.66$ was selected to fit the upper edge of the data in the region of small T. In Figure 4b, most of the data fall in the range $0.4 < a < 1$; noting this, a value of $R = 1.2$ has been selected so that the data in Figure 4a at large T fall between the lines for $a = 1$ and $a = 0.4$. A more rigorous fitting of these parameters is not warranted at present. We suggest that $\sin\phi$ is correct to $\pm5\%$ and R is correct to $\pm25\%$.

The experiments using coarse gouge are conspicuous in showing generally lower apparent friction and higher rates of thinning than the experiments using finer gouge or fractal gouge. This is consistent with the analysis presented, because the coarse gouge is expected to densify significantly as the large grains break down into smaller particles with a range of sizes that pack together more efficiently [e.g., *Wong*, 1990]. Quantitative estimates of the volumetric strain are given in the next section.

Further validation of the theory can be found by examining an individual experiment in greater detail. Figure 7 shows results from the experiment introduced in Figure 2, replotted on a diagram similar to Figure 4. These results match theoretical curves for a layer of constant thickness in which the variable a steadily increases towards 1. This increase reflects a change from thinning dominated by densification early in the experiment to thinning dominated by extrusion late in the experiment. The results in Figure 7 suggest that the flow law is adequate even for the early part of the experiment, where μ_a is quite small and the rate of layer thinning is quite large.

Volumetric strain. The assertion that the rate of extrusion is determined by GT also provides a way to estimate the volumetric strain (or densification) of the gouge. An increment in the yy component of strain can be divided into two contributions due to (1) densification and (2) extrusion at the rate determined by
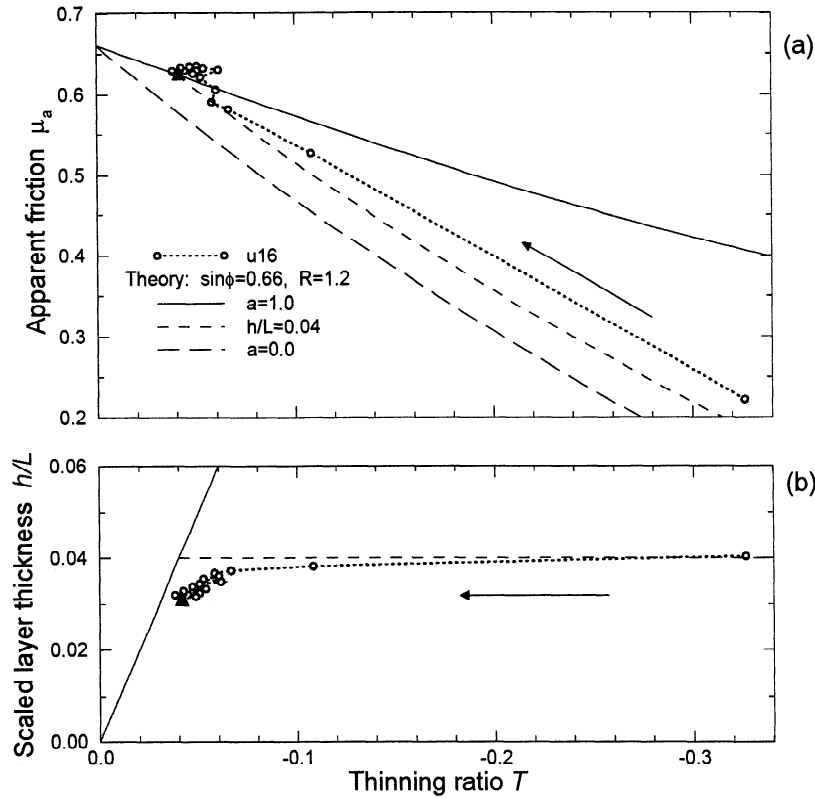
Figure 7. Results from experiment u16 (see Figure 2), replotted with the same layout as Figure 4. In both parts, the bold dashed line shows the progression of the rate of thinning in a single experiment from an initially high value to a lower, stable level. The arrows indicate the direction of progression, and the open circles show the actual data points at increments of 0.5 mm in shear displacement. The apparent friction in Figure 7a increases substantially during the experiment, and the layer thickness in Figure 7b decreases a little. The solid triangular symbols show the points that are plotted in Figure 4. The theoretical lines shown include the predictions for thinning due to extrusion only and densification only ($a = 0$ and $a = 1$), as in Figure 4. Also shown are lines for a layer of constant thickness ($h/L = 0.04$). Along these lines the rate of thinning varies from a large value, when densification is active, down to a smaller value, when the density is constant and only extrusion is active.

GT. In plane strain, the latter contribution is equal and opposite to $\delta\epsilon_{xx}$. From equation (43),

$$\delta\epsilon_{yy}^{GT} = -\frac{\delta X}{L} . \qquad (46)$$

Because any densification is attributed to uniaxial compression of the layer, the increment in volumetric strain Δ can be obtained from the difference between the total increment in thinning and that attributed to extrusion.

$$\delta\Delta = \delta\epsilon_{yy} - \delta\epsilon_{yy}^{GT} \qquad (47)$$

Using equations (4) and (46),

$$\delta\Delta = \frac{\delta h}{h} + \frac{\delta X}{L} . \qquad (48)$$

By integrating from an initial condition where $h = h_0$ and $X = 0$, the finite volumetric strain is given by

$$\Delta = -\ln\left\{\frac{h_0}{h(X)}\right\} + \frac{X}{L} . \qquad (49)$$

The volumetric strain Δ can be used to relate the initial and final porosities (f_0 and f) of the gouge:

$$f = 1 - (1 - f_0)\exp(-\Delta) . \qquad (50)$$

Figure 2d shows the progression of volumetric strain in a single experiment, calculated using equation (49) but plotted as a function of shear strain. Note that the volumetric strain rate is initially large but diminishes as the thinning ratio in Figure 2c approaches GT.

Using equation (50), the final volumetric strain $\Delta = -0.16$ shown in Figure 2d might correspond to a reduction in porosity from $f_0 = 0.35$ to $f = 0.24$. These values are reasonable but were not measured. It should be noted that by setting $f = 0$ in equation (50) we obtain a limit on the volumetric strain:

$$\Delta_{min} = \ln(1 - f_0) . \qquad (51)$$

This equation sets a lower limit of around -0.4 on Δ if the initial porosity is in the range $f_0 = 0.3$-0.35.

The calculated progression of volumetric strain is shown for all the experiments in Figure 8. We can
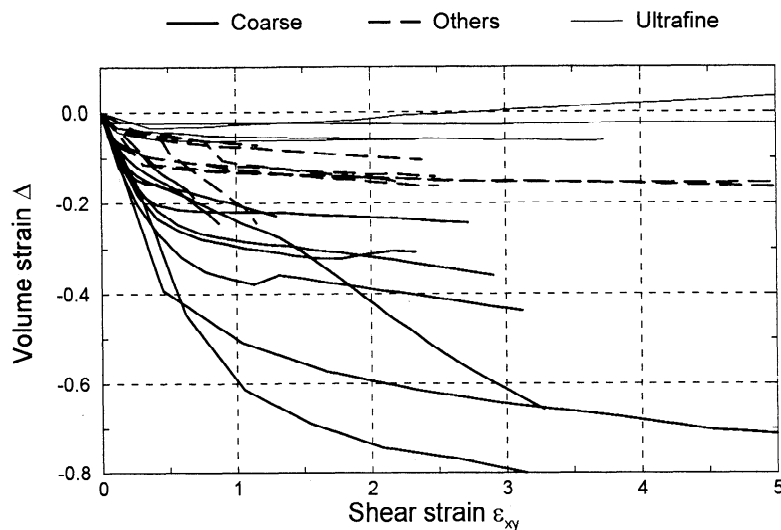
Figure 8. Estimates of volume strain from all the experiments. Each line is calculated using equation (49) and shows the progressive volumetric strain for a single experiment (see also Figure 2d). Data from experiments using a range of layer thickness are shown together by using the shear strain on the horizontal axis; lines for the thickest layers terminate at a shear strain of about 1, whereas those for the thinnest layers run out to strains in excess of 5. The light lines show data for the ultrafine gouge and typically show very little volume strain. The dashed lines show data for the medium, fractal, and Lopez gouge types and typically show a total volume strain of around −0.1. The heavy lines show data for the coarse gouge and show larger total volume strains. The estimates of volume strain for coarse gouge in thin layers may be unreliable (see text).

account for the trends shown by associating the process of densification with the evolution of the grain size distribution by fragmentation. *Biegel et al.* [1989] and *Marone and Scholz* [1989] demonstrated that gouge with a narrow range of grain sizes quickly develops a broad, power law grain size distribution by fragmentation when sheared. The fractal gouge is denser because the grains pack together more efficiently.

With one exception, the experiments using ultrafine gouge show minimal volumetric strain. This gouge has very small grains and also a reasonably large range in grain size. Many of the grains may be too small (1 μm) to fragment at the stress levels used in these experiments.

The experiments using coarse gouge show large amount of volume strain, passing well beyond our estimated limit of $\Delta = -0.4$ in some cases. This gouge has a grain size of nearly 1 mm and is observed to undergo a great deal of grain fragmentation during experiments. The two cases showing the largest volume strains are layers whose initial thickness was about one grain diameter, between grooved steel sample blocks. In these cases, the inital porosity is probably anomalously large, so that more densification is permissible. Also, with such thin layers, loss of small grains into the grooves of the rough steel sample blocks probably causes a significant amount of anomalous thinning.

In the experiments with medium, fractal, and natural Lopez gouges, the volumetric strain lies between the extremes set by the ultrafine and coarse gouges.

Discussion

Regardless of the details of the discussion that follows, it should be emphasized that mechanical properties of gouge layers or fault zones are more complicated than those of bare rock surfaces. The gouge in fault zones is distinct from the surrounding country rock and should be treated as a finite continuum. It is misleading to parameterize the material properties of a finite fault zone in terms of the conventional coefficient of friction, which is basically a surface property.

Internal Friction and Apparent Friction

It is evident from our results that a clear distinction must be made between the internal friction μ of gouge, a material property, and the apparent friction μ_a of a gouge layer, a property of the entire system. The internal friction is more familiar and is the foundation of a quantitative predictive framework, but it is the apparent friction that is usually measured and that has real external significance.

We certainly concur with the view presented by *Hobbs et al.* [1990] and *Byerlee and Savage* [1992] that the maximum apparent friction of a gouge layer or a fault zone is the sine of the angle of friction rather than its tangent. The apparent friction may, however, be significantly less than this upper limit. Previous measurements of the frictional strength of gouge layers therefore represent lower bounds on $\sin \phi$ rather than direct measurements of $\tan \phi$.

The apparent friction of a gouge layer in the laboratory is not uniquely determined by the internal friction. Our analysis of the relationship between the measured apparent friction and the inferred internal friction calls for additional information, namely, the rates of extrusion and densification of the gouge layer. Neither of these are directly observed in the double-direct-shear experiments, but both can be inferred from measurements of shear strain and layer thinning.

The interpretation of experiments of fault gouge in any experimental geometry should be conducted with these concepts in mind. They certainly apply to other double-direct-shear experiments and also to triaxial saw-cut and rotary shear experiments.

The effect of densification. It was is not possible to monitor the gouge density in the double-direct-shear apparatus used in this study; hence we have had to estimate the volumetric strain rate indirectly by using the concept of geometric thinning. For medium, fractal, and Lopez gouge, densification is inferred to be important during the initial stage of an experiment, up to a shear strain of about 0.3 (see Figures 2 and 8). For coarse gouge, densification is most rapid during this initial stage but may persist for somewhat longer.

In triaxial sawcut experiments the pore volume, and hence gouge densification, can be measured directly. Such measurements are presented by *Marone and Scholz* [1989] and *Marone et al.* [1990] and are used here to confirm qualitatively the validity of our assertions about gouge densification. The gouge used in those studies was equivalent to our coarse gouge, and most of their experiments used normal stresses of 100 MPa, significantly greater than the normal stress of 25 MPa used here.

They always observed significant porosity reduction up to shear strains of around 0.3 (note also that they use the engineering definition of shear strain; their values are halved to be consistent with the definition used here). A rough inspection of their data during these initial stages suggests that our value of around unity for the flow constant R, which controls the rate of densification with respect to shear strain in equation (39), is consistent with their data.

After this initial stage, porosity reduction is succeeded by dilation in their experiments at 100 MPa. This is inconsistent with our results for coarse gouge, where densification continues to larger shear strains. However, *Marone and Scholz* [1989] performed a single experiment at 20 MPa normal stress, which showed continuing porosity reduction out to shear strains in excess of unity; this result is consistent with our inferences about the densification of coarse gouge. Comparing the results at 100 MPa and 20–25 MPa, it appears that full densification of coarse gouge is accomplished with less shear strain as the normal stress increases, because grain fragmentation is more efficient.

The effects of extrusion and layer thickness. Even after the gouge has attained a constant density, the apparent friction continues to be affected by the process of extrusion. This effect can be misinterpreted as simply being due to layer thickness, whereas the important variable is the ratio of layer thickness to length. Refering to Figure 4, extrusion has a significant effect on the apparent friction of layers whose thickness exceeds perhaps one-twentieth of their length (a thinning ratio of −0.05).

Dieterich [1981] and *Biegel et al.* [1989] report a decrease in the apparent friction of gouge layers with increasing layer thickness in double-direct-shear experiments. Their observations are in qualitative agreement with those presented here. Our analysis indicates, however, that layer thickness is not the key variable; it is the rate of change of thickness with shear displacement that is quantitively related to the apparent friction. Only because thicker layers thin more rapidly is a correlation between layer thickness and apparent friction observed.

It is more difficult to monitor changes in the layer thickness precisely in triaxial sawcut experiments, because the sawcut cylinder is jacketed to isolate it from the fluid confining medium. However, as in our double-direct-shear results, the initial thickness of the gouge layer should provide an indication of the rate of thinning during the experiment. *Shimamoto and Logan* [1981] report the apparent friction of dolomite gouge layers with initial thicknesses of 0.5–2 mm. The normal stress and sample size (equivalent to to the layer dimension L here) were also varied. They find no significant variation in the apparent friction with layer thickness in these experiments. Their result is surprising in light of this study but may reflect a difference in the behavior of quartz and dolomite gouge. Alternatively, it may be that in the confined triaxial apparatus, the gouge layer has less tendency to extrude; layer thinning by extrusion is perhaps a peculiarity of the double-direct-shear geometry, wherein the edges of the gouge layers are unconfined.

Summers and Byerlee [1977] report triaxial sawcut experiments on layers with a range of different mineral compositions. In most of these experiments the layer was not granular gouge but instead an intact wafer of material sandwiched between granite sample blocks. It is not clear whether our analysis applies to such experiments, because the strain may not be distributed throughout the gouge layer.

In rotary shear experiments, extrusion in the sense we have described is impossible; gouge cannot escape from an annular layer in the circumferential direction of shearing. Radial extrusion can also be prevented by correctly choosing the radial confining pressure (T. Tullis, personal communication, 1992). Hence the apparent friction should be affected by only the initial process of densification. We discuss this further in the following section.

Strain Localization in Gouge Layers

The presence of a gouge layer leads to strain localization in a general sense, because the solid material to either side does not deform plastically. Localization of the strain within gouge layers and natural fault zones has been discussed by many authors [e.g., *Tchalenko*, 1970; *Mandl et al.*, 1977; *Byerlee et al.*, 1978; *Logan et*

al., 1979; *Groshong*, 1988; *Marone and Scholz*, 1989].
Oblique Riedel shears are usually described, and their
interpretation as Coulomb failure planes is well estab-
lished. Layer-parallel shears, termed Y-shears by *Lo-
gan et al.* [1979], are also often described. A recent,
detailed study by *Gu and Wong* [1994] provides quan-
titative documentation of the sequential appearance of
Riedel and Y-shears in triaxial sawcut experiments on
fine-grained gouge. The significance of both types of
slip plane is discussed here.

Riedel shears. The observation of continuing layer
thinning in our experiments has important implications
for the process of shear localization. In the latter part
of the experiments, the layer thinning is due to extru-
sion at constant density. This requires that strain be
distributed both along and across the entire layer.

Displacements on a population of conjugate Riedel
shears can produce the required strain field and satisfy
the Mohr-Coulomb failure condition. However, because
the Riedel shears are oblique to the layer, any single
shear plane can accommodate only a displacement that
is a small fraction of the layer thickness. The plane
must then be abandoned and a new plane activated.

For this reason, we argue that localization is inhib-
ited in these experiments. In gouge, like other granular
materials such as sandy soil, shear strain spontaneously
localizes into shear bands. However, the kinematic con-
straints imposed on gouge in a sheared layer are such
that localization cannot persist in one place for very
long.

Layer-parallel Y shears. The preceding argument
leads to a paradox when we acknowledge that Y-shears
are also observed in gouge layers. While Riedel shears
are the first evidence of localization, Y-shears emerge as
the shear strain becomes large. This is most obvious in
rotary shear experiments [e.g., *Mandl et al.*, 1977; *Blan-
peid et al.*, 1988] but has also been observed in double-
direct-shear and triaxial sawcut experiments with rel-
atively large shear displacements. Y-shears sometimes
form close to the boundary betwen the gouge and the
solid wall but are often in the middle of the gouge layer.

It appears to make sense that a single Y-shear should
form in a sheared layer, as it can accommodate indefi-
nite amounts of shear strain. A Y-shear is not, however,
optimally oriented for the stress field inferred here and
observed by *Mandl et al.* [1977]. If the applied shear
stress is sufficient to drive slip on a Y-shear, the opti-
mally oriented Riedel shears should be well past failure,
if the same coefficient of internal friction is used.

One of the assumptions made in the present analysis
must break down when Y-shears develop. Their devel-
opment may be involved with the development of het-
erogeneity within the gouge layer, as suggested by the
transition in frictional behavior observed by *Marone et
al.* [1992]. This heterogeneity might be in the stress
field, but it is perhaps more likely that the material
properties become heterogeneous. For example, a sub-
layer of finer-grained gouge might form, which for some
reason has a lower internal friction than does the rest
of the gouge. These explanations are far from precise,
and the formation of Y-shears invites further study.

The Rate Dependence of Apparent Friction

The success of our analysis of apparent friction invites
a brief discussion of its implications for the more subtle
issue of frictional stability.

Rate- and state-dependent friction laws [*Dieterich*,
1981; *Ruina*, 1983] are the accepted framework for
quantifying frictional stability, although for the most
part these laws are phenomenological. For bare sur-
faces, a reasonably precise micromechanical justification
for the phenomology has been proposed, on the basis of
the evolution of the population of asperities that pro-
vide the real contact between surfaces. Observations
of asperities between sliding lucite blocks provide di-
rect evidence of these micromechanical processes [*Kil-
gore and Dieterich*, 1992].

The micromechanics of rate dependence in the appar-
ent friction of a gouge layer is presumably more com-
plicated. The strain in a granular gouge layer may be
accommodated by grain fragmentation and rotation as
well as slip on intergranular asperities.

Experimental observations of gouge layers show that
the rate dependence of friction and the critical displace-
ment over which rate dependence evolves change with
shear strain [e.g., *Biegel et al.*, 1989; *Marone et al.*,
1992]. This presumably reflects a change in the balance
of mechanisms that accommodate strain. Our results
provide an indicator of these same mechanisms. For ex-
ample, when the rate of densification is high, grain frag-
mentation (a rate-strengthening process) is certainly
very active. As the rate of densification decreases, we
might expect to move toward rate-weakening behavior.

The evolution of strain localization discussed above
probably affects the charateristic displacement. If ex-
trusion is occurring, strain must be distributed through-
out the layer, whereas if a Y-shear forms, then strain is
localized within the layer; this transition probably leads
to a reduction in the critical displacement.

The Strength of Natural Fault Zones

Extrapolating from carefully controlled laboratory
conditions to natural fault zones is necessarily specu-
lative. The mechanical processes we have analyzed are,
however, sufficiently simple and general that there is
no reason not to expect similar conditions to give rise
to similar results on geological scales. We must there-
fore discuss the likelihood that anything resembling our
experimental conditions might arise in nature.

A motivation for such a discussion is the apparent
weakness of major crustal fault zones (see *Hickman*
[1991] for a review). Observations of the heat flow and
stress orientation associated with the San Andreas fault
in California suggest that the frictional strength of this
mature, active fault is low both in an absolute sense and
relative to other faults in the immediate vicinity. These
observations are most easily reconciled if the apparent
friction of the fault zone is reduced to around 0.1.

While the results reported here do not offer values
of apparent friction as low as 0.1, it is worth consider-
ing how large an effect the processes of extrusion and
densification might have in nature.

Extrusion. To obtain an apparent friction of 0.1 for a layer of quartz gouge at constant density would require a thinning ratio of around -2. It seems very unlikely that such a value would arise, or even less persist, in nature.

Furthermore, to appeal to any effect of extrusion in a natural fault zone requires an explanation of the fate of the extruded gouge. The fault zone presumably forms a closed system, so layer thinning in one place must be balanced by layer thickening nearby. The apparent friction of a thickening layer can be obtained using the same analysis (e.g., equation (24)) with positive values of the thinning ratio T. For values of T less than about 0.2, a thickening layer strengthens with T at about the same rate that a thinning layer weakens. Therefore a closed fault zone containing complementary thinning and thickening regions would have an average apparent friction of around $\sin \phi$. This value is 0.66 in the experiments presented here, far in excess of the low apparent friction suggested by the heat flow and stress orientation around "weak" faults.

There is also some possibility of lateral extrusion in a fault zone. We have not analyzed the mechanical consequences of such behavior in detail. If the gouge could somehow escape, perhaps through upward extrusion to the surface, layer thinning would occur without complementary layer thickening, and the fault zone would be weakened.

Densification. The densification effect is also clearly not sustainable in a uniform fault zone experiencing continuing displacement. It may, however, feature in the mechanics of a fault zone that is continuing to widen with time, incorporating more gouge by fragmentation of the surrounding country rocks. It is conceivable that the extremely low values of apparent friction seen in the early parts of our experiments (see Figure 7) might apply in such circumstances. It would be possible to develop the present analysis to describe such circumstances, with the introduction of additional constitutive assumptions for the rate of widening of the fault zone and the initial density of new gouge. The analysis should then, however, include the effects of dilation in the country rocks that would accompany fragmentation. By analogy with the preceding discussion of extrusion, complementary thinning due to densification and thickening due to dilatant fragmentation would probably cancel each other out.

Conclusions

1. Layer thinning observed in double-direct-shear experiments on granular quartz gouge can be attributed to extrusion and densification of the gouge layer. Thicker layers generally display more thinning and lower apparent friction.

2. In analyzing the process of extrusion, the observed strain can be used to estimate the orientation of the stress tensor and hence relate the apparent friction of the layer to the internal friction of the gouge. The assumptions of plane strain and of coaxiality of deviatoric stress and plastic strain rate are made in this analysis.

Allowing only for extrusion, a constant value of internal friction ($\tan \phi = 0.88$) that fits experiments with less thinning systematically overpredicts the apparent friction for experiments with more thinning.

3. Extending the analysis to include thinning due to densification can reduce the predicted apparent friction (for the same value of internal friction) and improve the fit to the observations, particularly for coarse gouge in which considerable fragmentation occurs. This analysis introduces one additional material parameter, in the form of the constant R in a flow law relating volumetric strain to shear strain and the state of stress.

4. The rate of thinning due to extrusion is probably controlled by the ratio of layer thickness to the overall layer length ("geometric thinning"). This effect may be peculiar to the double-direct-shear experimental configuration.

5. While is unlikely that the processes observed and analyzed here are directly applicable to natural fault zones, the mechanical analysis described here is quite general and should apply to experiments on gouge in other experimental configurations.

References

Biegel, R. L., C. G. Sammis, and J. H. Dieterich, The frictional properties of a simulated gouge having a fractal particle distribution, *J. Struct. Geol.*, *11*, 827–846, 1989.

Blanpied, M. L., T. E. Tullis, and J. D. Weeks, Textural and mechanical evolution of granite gouge in high-displacement sliding experiments (abstract), *Eos Trans. AGU*, *69*, 1478, 1988.

Britto, A. M., and M. J. Gunn, *Critical State Soil Mechanics via Finite Elements*, 488pp., Ellis Horwood, Chichester, England, 1987.

Byerlee, J. D., Friction, overpressure and fault normal compression, *Geophys. Res. Lett.*, *17*, 2109–2112, 1990.

Byerlee, J. D., and J. C. Savage, Coulomb plasticity within the fault zone, *Geophys. Res. Lett.*, *19*, 2341–2344, 1992.

Byerlee, J. D., V. Mjachkin, R. Summers, and O. Voevoda, Structures developed in fault gouge during stable sliding and stick-slip, *Tectonophysics*, *44*, 161–171, 1978.

Dieterich, J. H., Constitutive properties of faults with simulated gouge, in *Mechanical Behavior of Crustal Rocks*, *Geophys. Monogr. Ser.*, vol. 24, edited by N. L. Carter et al., pp. 103–120, AGU, Washington, D.C., 1981.

Engelder, J. T., J. M. Logan, and J. Handin, The sliding characteristics of sandstone on quartz fault-gouge, *Pure Appl. Geophys.*, *113*, 69–86, 1975.

Green, G. E., and A. W. Bishop, A note on the drained strength of sand under generalized strain conditions, *Geotecnique*, *19*, 144–149, 1969.

Groshong, R. H., Low-temperature deformation mechanisms and their interpretation, *Geol. Soc. Am. Bull.*, *100*, 1329–1360, 1988.

Gu, Y., and T.-F. Wong, Development of shear localisation in simulated quartz gouge: Effect of cumulative slip and gouge particle size, *Pure Appl. Geophys.*, in press, 1994.

Hickman, S., Stress in the lithosphere and the strenth of active faults, U.S. National Report to the International Union of Geodesy and Geophysics 1987–1990, *Reviews of Geophysics Supplement*, 759–775, 1991.

Hill, R., *The Mathematical Theory of Plasticity*, 355pp., Clarendon Press, Oxford, England, 1960.

Hobbs, B. E., A. Ord and C. Marone, Dynamic behavior of rock joints, in *Proceedings of the International Symposium on Rock Joints*, edited by N. R. Barton and O. Stephansson), pp. 435–445, Balkema, Rotterdam, 1990.

Kilgore, B. D., and J. H. Dieterich, Video images of micromechanical fault processes (abstract), *Eos Trans. AGU*, *73*, 526, 1992.

Linker, M. F., and J. H. Dieterich, Effects of variable normal stress on rock friction: observations and constitutive equations, *J. Geophys. Res.*, *97*, 4923–4940, 1992.

Logan, J. M., M. Friedman, N. Higgs, C. Dengo, and T. Shimamoto, Experimental studies of simulated gouge and their application to studies of natural fault zones, in *Analysis of actual fault zones in bedrock*, *U. S. Geol. Surv. Open File Rep. 79-1239*, 276–304, 1979.

Mandl, G., *Mechanics of Tectonic Faulting: Models and Basic Concepts*, 407pp., Elsevier, New York, 1988.

Mandl, G., L. N. J. de Jong, and A. Maltha, Shear zones in granular material, *Rock Mech.*, *9*, 95–144, 1977.

Marone, C., and B. Kilgore, Scaling of the critical slip distance for seismic faulting with shear strain in fault zones, *Nature*, *362*, 618–621, 1993.

Marone, C., and C. H. Scholz, Particle-size distribution and microstructures within simulated fault gouge, *J. Struct. Geol.*, *11*, 799–814, 1989.

Marone, C., C. B. Raleigh, and C. H. Scholz, Frictional behavior and constitutive modeling of simulated fault gouge, *J. Geophys. Res.*, *95*, 7007–7025, 1990.

Marone, C., B. E. Hobbs, and A. Ord, Coulomb constitutive laws for friction: Contrasts in frictional behavior for distributed and localized shear, *Pure Appl. Geophys.*, *139*, 195–214, 1992.

Rice, J. R., Fault stress states, pore pressure distributions, and the weakness of the San Andreas Fault, in *Fault Mechanics and Transport Properties of Rocks*, edited by B. Evans and T.-F. Wong, pp. 475–503, Academic, San Diego, Calif., 1992.

Ruina, A. Slip instability and state variable friction laws, *J. Geophys. Res.*, *88*, 10359–10370, 1983.

Sammis, C. G., and R. L. Biegel, Fractals, fault-gouge, and friction, *Pure Appl. Geophys.*, *131*, 255–271, 1989.

Sammis, C. G., G. C. P. King, and R. L. Biegel, The kinematics of gouge deformation. *Pure Appl. Geophys.*, *125*, 777–812, 1987.

Scott, D. R., D. Lockner, C. G. Sammis and J. Byerlee, Triaxial testing of Lopez fault gouge at 150 MPa mean effective stress, *Pure Appl. Geophys.*, in press, 1994.

Shimamoto, T., and J. M. Logan, Effects of simulated fault gouge on the sliding behavior of Tennessee Sandstone: Nonclay gouges, *J. Geophys. Res.*, *86*, 2902–2914, 1981.

Summers, R., and J. D. Byerlee, Summary of results of frictional sliding studies, at confining pressures up the 6.98 kbar, in selected rock materials, *U. S. Geol. Surv. Open File Rep. 77-142*, 129 pp., 1977.

Tchalenko, J. S., Similarities between shear zones of different magnitudes, *Geol. Soc. Am. Bull.*, *81*, 1625–1640, 1970.

Tullis, T. E., M. L. Blanpied, and J. D. Weeks, The velocity dependence of granite friction with and without simulated gouge (absract), *Eos Trans. AGU*, *70*, 1302, 1989.

Wong, T.-F., Mechanical compaction and brittle-ductile transition in porous sandstones, in Deformation Mechanisms, Rheology, and Tectonics, edited by R. J. Knipe and E. H. Rutter, *Geol. Soc. Spec. Publ. 54*, pp. 111–122, London, 1990.

C. J. Marone, Department of Earth, Atmospheric and Planetary Sciences, Massachusetts Institute of Technology, 54-724, Cambridge, MA 02139

C. G. Sammis, Department of Geological Sciences, University of Southern California, Los Angeles, CA 90089-0740

D. R. Scott, Department of Geological Sciences, University College London, Gower Street, London WC1E 6BT, U.K.